Chemical Engineering Journal 486 (2024) 150170

Contents lists available at ScienceDirect

Chemical Engineering Journal

journal homepage: www.elsevier.com/locate/cej

Ni-based bimetallic catalysts for hydrogen production via (sorption-enhanced) steam methane reforming

Siqi Wang [a,*], Ziqi Shen [a], Amin Osatiashtiani [b], Seyed Ali Nabavi [a], Peter T. Clough [a,*]

[a] Energy and Sustainability Theme, Cranfield University, Cranfield, Bedfordshire MK43 0AL, UK
[b] Energy and Bioproducts Research Institute (EBRI), College of Engineering and Physical Sciences, Aston University, Aston Triangle, Birmingham B4 7ET, UK

ARTICLE INFO

Keywords:
Bimetallic catalyst
Hydrogen production
Steam methane reforming
Sorption-enhanced steam methane reforming
Microkinetic modelling

ABSTRACT

The catalytic performance of a monometallic Ni/Al_2O_3 and three bimetallic catalysts (Ni_3M_1/Al_2O_3, with M = Cu, Fe, and Ge) for the (sorption-enhanced) steam methane reforming reaction was evaluated. Ni_3Cu_1/Al_2O_3 was found to be the optimal catalyst in terms of methane conversion, hydrogen yield, and purity. Ge also has a promoting effect on the monometallic Ni catalyst, whereas the addition of Fe negatively influenced its performance. Physico-chemical characterization of the materials indicated the formation of alloys upon activation of the materials with hydrogen. The addition of Cu increased the surface area and metal dispersion, and improved the overall morphology of the catalyst. The experimental observations were also supported by a numerical study combining Density Functional Theory-based calculations and Microkinetic modelling of the SMR process. Ni_3Cu_1 and Ni_3Ge_1 were calculated to have a similar level of catalytic activity as Ni, whereas Ni_3Fe_1 was unsuitable for the reaction. The SMR reaction was further improved by adding calcium oxide as the CO_2 sorbent, which increased methane conversion, CO selectivity, hydrogen yield, and hydrogen purity. The highest methane conversion of 97 % was achieved by Ni/Al_2O_3 and Ni_3Cu_1/Al_2O_3 at 700 °C.

1. Introduction

Hydrogen is one of the most promising alternatives to fossil fuels for several industrial applications because of its clean combustion products and high-grade heat generated upon combustion. Currently, Steam Methane Reforming (SMR) is the most predominant industrial process used for hydrogen and syngas production. The SMR reaction (Eq. (1)) takes place at high temperature and pressure (typically between 700 and 1000 °C and 14–20 bar [1]) in the presence of a catalyst and is accompanied by the Water-Gas Shift (WGS) reaction (Eq. (2)), which further enhances hydrogen production. Removal of the CO_2 produced in this process is usually carried out through in-process capture or endpoint capture using technologies like amine-based solvent scrubbing or Pressure Swing Adsorption [2]. In recent years, a novel technology – sorption-enhanced steam methane forming (SESMR) – has been proposed, which integrates *in-situ* CO_2 capture with the conventional SMR process (Eq. (3) and Eq. (4)). The integration of the CO_2 capture unit with the reforming reactor enhances hydrogen production by shifting the equilibrium of the reactions and reduces the overall cost of the system as a more compact process unit is employed [3].

$$\text{Steam methane reforming}: \ CH_4 + H_2O \leftrightarrow CO + 3H_2 \ \ \Delta H^{\circ}_{298} = +206\,\text{kJ/mol} \quad (1)$$

$$\text{Water} - \text{gas shift}: \ CO + H_2O \leftrightarrow CO_2 + H_2 \ \ \Delta H^{\circ}_{298} = -41\,\text{kJ/mol} \quad (2)$$

$$CO_2 \text{ capture and sorbent regeneration}: \ CO_2 + CaO \leftrightarrow CaCO_3 \ \ \Delta H^{\circ}_{298} = -178\,\text{kJ/mol} \quad (3)$$

Abbreviations: BEP, Brønsted–Evans–Polanyi; BET, Brunauer–Emmett–Teller; BJH, Barrett-Joyner-Halenda; DFT, Density Functional Theory; EDX, Energy dispersive X-ray analysis; GGA, Generalized gradient approximation; GHSV, Gas hourly space velocity; MKM, Microkinetic modelling; PAW, Projection augmented wave; PBE, Perdew–Burke–Ernzerhof; SEM, Scanning electron microscopy; SESMR, Sorption-enhanced steam methane reforming; SMR, Steam methane reforming; TGA, Thermogravimetric analysis; UBI-QEP, Unity bond index-quadratic exponential potential; vol.%, Volume percentage; wt.%, Weight percentage; XPS, X-ray photoelectron spectroscopy; XRD, X-ray diffraction; XRF, X-ray fluorescence analysis.

* Corresponding authors.
E-mail addresses: Siqi.Wang2019@cranfield.ac.uk (S. Wang), P.T.Clough@cranfield.ac.uk (P.T. Clough).

https://doi.org/10.1016/j.cej.2024.150170
Received 3 November 2023; Received in revised form 2 February 2024; Accepted 3 March 2024
Available online 4 March 2024

$$\text{Overall equation of SESMR}: \ CH_4 + H_2O + CaO \leftrightarrow CaCO_3 + 4H_2 \ \ \Delta H^{\circ}_{298} = -13\,\text{kJ/mol} \quad (4)$$

Both SMR and SESMR require the presence of a catalyst to proceed at a sufficient rate. Commercial Ni-based catalysts are the most commonly used because of their high catalytic activity, good availability and relatively low price. However, some of the major issues associated with Ni-based materials include sintering, carbon deposition, and sulphur poisoning. The addition of a second metallic element to enhance the performance Ni-based catalysts has been extensively investigated, and noble metals (including Ru, Rh, Pd and Pt) have been found to be excellent promoters [4]. Although these materials have high catalytic activity and good stability, their application to industrial processes is limited by the cost of noble metals. Researchers have therefore turned to non-noble metal promoters and bimetallic catalysts in search of cost-effective alternatives. Xu et al. [5] developed a microkinetic model based on the elementary reaction steps of SMR and screened a list of ~500 bimetallic alloys based on their adsorption energies, thermodynamic stability, oxide stability, and price. They concluded that Ni_3Fe_1, Co_3N_i, and Ni_3X_1 (X = Ge, As, and Sb) are potentially good candidates for SMR at high temperatures. A similar approach was employed by Liu et al. [6] to screen a large database containing 5,000 adsorption energies on different bimetallic surfaces and adsorption sites. They identified 48 stable and inexpensive bimetallic alloys that are potentially active for SMR, among which Ni_3Cu_1, Ni_1Fe_1, and Ni_3Co_1 are present.

Khzouz et al. [7] tested the performance of a Ni-Cu/Al_2O_3 catalyst for low temperature SMR and concluded that Cu acts as a stabilizer and improves the overall activity of the bimetallic material by inhibiting coke formation. Huang and Jhao [8] carried out SMR tests with samaria-doped ceria supported Ni-Cu catalyst and attributed the enhanced performance to the promoting effect of Cu on the WGS reaction. MgO-supported Ni-Cu and Ni-Fe catalysts were tested for both steam and dry methane reforming by Djaidja et al. [9], results showed that although the addition of Cu and Fe decreased the overall catalytic activity, the stability of the materials was improved with less carbon formation. On the other hand, Ni-Ge-based catalysts have been seldomly employed for reforming processes. However, germanium-based catalysts have been proven to be active for hydrogen production. Furukawa et al. [10] used Ni-Ge/SiO_2 and Co-Ge/SiO_2 as catalysts for hydrogen production from ammonia-borane and it exhibited higher catalytic activity compared to Ni/SiO_2 and Co/SiO_2. This promoting effect was attributed to the enhanced reducibility of the bimetallic catalysts and the enrichment of electrons in Ni and Co through alloy formation. Moreover, germanium-based catalysts have also been found to be sulphur resistant. Garetto et al. [11] tested the sulphur-resistant ability of monometallic Pt and bimetallic Pt-Ge catalysts, using thiophene as the source of sulphur. They concluded that the addition of Ge improved the sulphur resistance of the catalyst by decreasing the density of charge of the alloy and weakening the bond strength between metallic elements and electrophilic sulphur. It is therefore of interest to investigate the performance of Ni-Ge-based bimetallic catalyst for SMR, as it has been predicted to have a high activity [5]. The addition of Ge can also potentially improve the sulphur resistance of the bimetallic Ni-Ge catalyst. This is particularly beneficial for future large-scale application of this novel bimetallic catalyst, as the presence of sulphur-containing species (e.g. H_2S, thiophene) is usually inevitable in the natural gas stream under industrial SMR conditions, and can easily deactivate conventional Ni-based catalysts [12,13]. Although Ni-As and Ni-Sb alloys were also predicted to be active for SMR, they were excluded from this study due to the toxicity of As and Sb.

The performance of bimetallic catalysts under SESMR conditions has also been studied. Ghungrud et al. [14] tested novel hydrotalcite-supported Ni-Co catalysts and reported that the methane conversion increased with Co loading in the material, which was attributed to the enhancement of the WGS reaction by Co. The Ni-Co bimetallic catalysts were further promoted by Ce. A higher metal dispersion and better metal-support interaction were achieved, resulting in a maximum methane conversion of 95.7 %. Similarly, hydrotalcite-supported Ni-Ce and Ni-Zr catalysts were studied by Dewoolkar et al. [15]. The materials achieved a high methane conversion of approximately 96 %. The coke resistance of the catalysts was also enhanced due to the increase in surface area and surface basicity with the addition of Ce and Zr. To the best of the author's knowledge, the use of Ni-Cu, Ni-Fe, and Ni-Ge bimetallic catalysts for SESMR has not been studied before. It is therefore of interest to test these novel materials under SESMR conditions to evaluate their performance and investigate the effects of the CO_2 sorbent on their catalytic activity.

In this study, the catalytic performance of a monometallic Ni/Al_2O_3 catalyst and a series of Ni-based bimetallic catalysts (noted Ni_3M_1/Al_2O_3, with M = Cu, Fe, and Ge) were evaluated and compared. The materials were tested under both SMR and SESMR conditions, and their catalytic activity was further evaluated with ab-initio Density Functional Theory (DFT)-based simulations and Microkinetic modelling (MKM). This combined experimental and numerical study of bimetallic catalysts provides insight into the promoting effect of several cost-effective and widely available non-noble metals and their potential as novel alternatives to conventional Ni-based materials. This work also aims to provide an experimental verification of previous high-throughput screening studies and is also the first-ever attempt to experimentally test Ni-Ge-based material as an SMR catalyst.

2. Methodology

2.1. Catalyst synthesis

Ni/Al_2O_3, Ni_3Cu_1/Al_2O_3 and Ni_3Fe_1/Al_2O_3 catalysts were synthesized by impregnating the alumina support (gamma-phase, bimodal, Alfa Aesar) with the aqueous solution of nickel nitrate hexahydrate ($Ni(NO_3)_2{\cdot}6H_2O$, 99 %, Thermo Scientific Chemicals), copper nitrate hemipentahydrate ($Cu(NO_3)_2{\cdot}2.5H_2O$, 98 %, Thermo Scientific Chemicals) and iron nitrate nonahydrate ($Fe(NO_3)_9{\cdot}9H_2O$, 99 %, Thermo Scientific Chemicals). Appropriate amount of metal precursors was dissolved in deionised water so that the total metal loading in the reduced samples was equal to 10 wt%, and the Ni:Cu or Ni:Fe molar ratio was equal to 3:1. Ni_3Ge_1/Al_2O_3 was synthesized by impregnating the alumina support and GeO_2 powder (Germanium (IV) oxide, 99.9999 %, Thermo Scientific Chemicals) with appropriate amount of nickel nitrate solution, so that the total metal loading in the reduced samples was equal to 10 wt %, and the Ni:Ge molar ratio was equal to 3:1.

The solutions were then agitated in an ultrasonic tank for 3 h at 60 °C and dried in a static oven overnight. The samples were then calcined at 500 °C for 4 h with a heating rate of 5 °C/min, followed by hydrogen reduction at 600 °C (Ni/Al_2O_3 and Ni_3Cu_1/Al_2O_3) or 800 °C (Ni_3Fe_1/Al_2O_3 and Ni_3Ge_1/Al_2O_3).

2.2. Characterization

The catalysts were characterized using different techniques, including X-ray fluorescence spectroscopy (XRF), Scanning electron microscope (SEM) and energy dispersive X-ray analysis (EDX), N_2 physisorption, H_2 pulse chemisorption, X-ray diffraction (XRD), X-ray photoelectron spectroscopy (XPS) and Thermogravimetric analysis (TGA).

XRF analysis was carried out using a micro-XRF Bruker M6 Jetstream. Quantification was done using Fundamental parameters, with data acquired at 30 kV and 600 μA.

SEM-EDX analysis was carried out using the TESCAN VEGA 3 scanning electron microscope.

N_2 adsorption and desorption isotherms were obtained using the Micromeritics 3 Flex instrument. Prior to the physisorption tests, the

samples were degassed at 400 °C for 5 h with a heating rate of 10 °C/min to remove any moisture or impurities. The surface area was calculated using the Brunauer–Emmett–Teller (BET) equation, and the total pore volume and median pore radius were obtained from the Barrett-Joyner-Halenda (BJH) method.

A Micromeritics 3Flex was also used to perform pulse H_2 pulse chemisorption tests. Prior to the chemisorption measurements, pure hydrogen stream was flowed over one gram of fresh catalyst for 30 min to fully reduce the catalyst. The samples were then degassed in a N_2 stream and cooled down to 30 °C. Loop H_2 gas was pulsed over the sample for 10 times or until the area of the peaks was stable, indicating no further adsorption of H_2 by the sample.

XRD results were obtained with the Siemens D5005 X-ray Diffractometer using Cu Kα radiation. The reduced samples were crushed into a powder and scanned in the 2θ range of 30°–80° with a step size of 0.02°.

XPS analysis was carried out using a Thermofisher ESCALAB 250 electron spectrometer, which featured a hemispherical sector energy analyser. An Al Kα X-ray source with a single energy level was employed to optimise resolution. The experiments maintained a source excitation energy of 15 KeV, an emission current of 6 mA, an analyser pass energy of 20 eV, a step size of 0.1 eV, and a dwell time of 50 ms. Throughout the examinations, the spectrometer consistently maintained a base pressure better than 5×10^{-10} mbar, ensuring that all recorded signals were originated from the sample surface.

TGA of the used catalysts was carried out using a Perkin Elmer TGA 8000. Prior to the TGA tests, all samples were reduced by hydrogen and degassed for 24 h to ensure no metal oxides or impurities were present. Approximately 20 mg of sample was oxidized in air while being heated from 30 to 1000 °C with a heating rate of 10 °C/min. The change in sample weight during the oxidation process is equal to difference between the weight loss due to carbon combustion, and the weight increase due to metal oxidation. The degree of carbon formation is evaluated using the following equation:

$$m_{initial} + m_{oxidation} - m_{carbon} = m_{final} \tag{5}$$

$$\text{carbon amount}\,(wt.\%) = \frac{m_{carbon}}{m_{initial}} \tag{6}$$

Where $m_{initial}$ is the initial weight of the sample used for TGA, m_{final} is the final weight of the sample after TGA, $m_{oxidation}$ is the weight gained due the oxidation of metal in the air flow, and m_{carbon} is the weight reduced due to the combustion of carbon. Both $m_{initial}$ and m_{final} were measured directly by the balance of the TGA instrument. $m_{oxidation}$ was calculated using results from the XRF analysis (to determine the weight of each metal in the sample) and by assuming that all active metals (Ni, Cu, Fe, and Ge) are fully oxidised by the end of the TGA test. The carbon amount is defined as the amount of carbon present in the sample.

TGA of the used sorbent from the SESMR tests (with T = 700 °C) was also carried out to determine the amount of coke deposited on the sorbent material. Samples of used sorbent were heated from 30 °C to 800 °C in air flow with a heating rate of 10 °C/min. The TGA test of used sorbent consists of three main mass loss stages, which is considered to be typical for air TGA test of calcium oxide powders with coke deposition [16]. The first mass loss stage between 100 and 150 °C is due to the release of moisture. The second stage at around 450 °C is due to the decomposition of $Ca(OH)_2$, the sample weight by the end of this stage is noted m_1. The final stage between 600 and 700 °C is due to the combustion of deposited coke, and the sample weight by the end of this stage is noted m_2.

The amount of carbon deposited on the sorbent is calculated using the equation below:

$$m_{carbon}(wt.\%) = \frac{m_1 - m_2}{m_1} \tag{7}$$

A more intuitive visual representation of the TGA curves with numerical values can be found in section 3.3.

2.3. Activity test

A fixed bed reactor described by Shen et al. [17] was used to test the catalytic activities of Ni/Al_2O_3, Ni_3Cu_1/Al_2O_3, Ni_3Fe_1/Al_2O_3 and Ni_3Ge_1/Al_2O_3 catalysts under SMR and SESMR conditions.

2.3.1. Catalytic activity test for SMR

Approximately 2.5 g of catalysts was introduced at the centre of the reactor. The catalysts were reduced under a fixed gas flow of 10 % hydrogen (balanced with nitrogen) under 600 °C until no water was observed by the humidity probe (Vaisala HMT330 series) in the exhaust gas line. A gaseous feedstock of 10 vol% methane in nitrogen was then passed through the fed after a stable water content was generated in the system through an HPLC pump (Jasco, model PU1586). The operating temperatures of catalyst activity tests were controlled, ranging from 600 °C to 800 °C. The exhaust gases were analysed to determine the actual gas composition in a dry basis via a bundle of gas analysers (ADC MGA3000 model). All tests were carried out under atmospheric pressure, while a GHSV of 15,000 h^{-1} was chosen.

2.3.2. Catalytic activity test for SESMR

For SESMR, limestone (Longcliffe) was selected to be the sorbent material. The limestone was sieved to control the particle size to be in the range of 315 to 400 μm. In a typical SESMR test, approximately 3 g of sorbent was mixed with 2.5 g of catalysts and then the mixture was placed in the middle of the reactor using a quartz liner. The materials were sufficiently vibrated so that better contact could be achieved between the catalyst pellets and the sorbent particles. The catalyst/sorbent mixture was activated under the same hydrogen flow for SMR but at 850 °C. The mixture was considered to be fully activated when there was no water generation and no carbon dioxide was detected, which indicates the complete reduction of the catalyst and the complete calcination of the limestone. The SESMR tests were carried out at 600, 650, and 700 °C, as CO_2 adsorption occurs at temperatures lower than 760 °C [18], and the process shifts from SESMR to the conventional SMR at higher temperatures. Methane conversion, hydrogen yield, hydrogen purity, and CO selectivity were calculated based on the pre-breakthrough stage [19], and the averaged data are presented in this paper. Because of the sorbent, a lower operating temperature was chosen, which was controlled to be between 600 and 700 °C. The sorbent was disposed of after each test and for each SESMR test, only one temperature was selected. The same GHSV and pressure as the SMR tests were applied for all SEMSR tests.

With the gas composition data collected, methane conversion, hydrogen yield, hydrogen purity, and carbon monoxide selectivity were determined via the equations below:

$$CH_4\ \text{conversion} = \frac{CH_4\ \text{in} - CH_4\ \text{out}}{CH_4\ \text{in}} \tag{8}$$

$$H_2\ \text{yield} = \frac{4 \times H_2\ \text{out}}{CH_4\ \text{in}} \tag{9}$$

$$H_2\ \text{purity} = \frac{H_2\ \text{out}}{CH_4\ \text{out} + H_2\ \text{out} + CO\ \text{out} + CO_2\ \text{out}} \tag{10}$$

$$CO\ \text{selectivity} = \frac{CO\ \text{out}}{CO\ \text{out} + CO_2\ \text{out}} \tag{11}$$

Methane conversion under thermodynamic equilibrium conditions was obtained using FactSage software. FactSage equilibrium calculation was carried out under batch conditions. The same conditions as the experimental SMR tests were used: atmospheric pressure, steam to carbon ratio of 3 and temperatures of 600, 700 and 800 °C. However, it should be noted that FactSage can only simulate the gas compositions thermodynamically, assuming no influence or presence of catalysts/sorbent and the materials were perfectly mixed.

2.4. Density Functional Theory

All DFT-based calculations in this work were carried out using the Quantum Espresso software package [20]. The projector augmented wave (PAW) method [21] was used to simulate the interactions between the electrons and the ions. The generalized gradient approximation (GGA) with the Perdew–Burke–Ernzerhof (PBE) functional was used to describe the exchange correlation [22]. The plane wave cutoff energy was set to be 400 eV. A Monkhorst-Pack $3 \times 3 \times 1$ k-point grid was used to sample the Brillouin zone. Spin polarization effects were taken into account for magnetic elements. The convergence criteria for force and energy were set to be 0.025 eV/Å and 10^{-5} eV, respectively. All catalysts were simulated by a four-layer $p(2 \times 2)$ slab model, with the top two layers and the adsorbate relaxed, and the bottom two layers fixed. The two neighbouring layers in the z-direction were separated by a 10 Å vacuum. The adsorption energy, E_{ads}, is calculated as below:

$$E_{ads} = E_{ads*slab} - E_{ads} - E_{slab} \quad (12)$$

Where $E_{ads*slab}$ is the total energy of the slab with the absorbate, E_{ads} is the total energy of the isolated phase adsorbate, and E_{slab} is the total energy of the clean slab.

All gas phase species were modelled by placing the molecule in a cube with the lattice parameters of $a = 20\text{Å}, b = 20.5\text{Å}, c = 21\text{Å}$. A Monkhorst-Pack $1 \times 1 \times 1$ k-point grid was used to sample the Brillouin zone.

2.5. Microkinetic modelling

The microkinetic model was implemented using the descriptor-based analysis package CatMAP [23]. The model was constructed using the elementary steps of the SMR reaction, and reaction energetics obtained from DFT calculations, combined with the unity bond index-quadratic exponential potential (UBI-QEP) method and the Brønsted–Evans–Polanyi (BEP) relationship. The model was built based on the adsorption on 7 transition metal surfaces, including Rh(1 1 1), Ni (1 1 1), Cu(1 1 1), Fe(1 1 0), Pd(1 1 1), Pt(1 1 1), and Au(1 1 1). Detailed information on the reaction steps and energetics can be found in Supplementary Information.

3. Results and discussion

3.1. Characterization of fresh catalysts

3.1.1. XRF analysis

The XRF analysis was carried out to determine the actual metal loading and Ni:M ratio of the samples (Table 1). The actual metal loading of all samples is very close to the theoretical value of 10 %, with errors less than 6.3 %. The Ni:Cu and Ni:Ge ratios were measured to be 2.69: 1 and 2.7: 1, which are close to the theoretical value of 3: 1. However, the measured Ni:Fe ratio is significantly lower than the theoretical value. This agrees with the observation during the catalyst synthesis process – nickel nitrate has a higher water solubility compared with iron nitrate, making it easier to thoroughly penetrate the alumina pellets in the liquid form during the heated agitation process. As XRF is a surface technology, Fe segregated on the outer layer of the support resulted in a higher iron concentration.

Table 1
Theoretical and measured total metal loading and Ni:M ratio.

	Total metal loading (wt.%)		Ni:M ratio	
	Theoretical	Measured	Theoretical	Measured
Ni/Al_2O_3	10	9.88	–	–
Ni_3Cu_1/Al_2O_3		10.02	3: 1	2.79: 1
Ni_3Fe_1/Al_2O_3		9.37	3: 1	2.01: 1
Ni_3Ge_1/Al_2O_3		10.58	3: 1	2.67: 1

3.1.2. SEM-EDX analysis

The SEM images of the fresh calcined catalysts are presented in Fig. 1. The alumina support consists of interconnecting pores which allows for the efficient diffusion of reaction gases. All catalysts exhibit very similar morphological features, with a uniform distribution of metal particles on the support. The size of the particles is in the range of 5–30 μm. The spatial distribution of the active metals within the support was evaluated using EDX. The elemental mapping and the composition of the scanned area are presented in Fig. 2. It is evidenced that for all samples, the active metals are evenly distributed within the support with no apparent phase segregation or agglomeration. Cu and Ge were dispersed within the support with the desired ratio, meaning that a uniform layer of bimetallic species has been formed. However, it should be noted that the Ni:Fe ratio at the inner section of the Ni_3Fe_1/Al_2O_3 sample is lower than the theoretical value of 3: 1 (Fig. 2 (c)). This is consistent with the observation stated in 3.1.1 that Ni penetrates the alumina support more easily compared with Fe, and therefore is more evenly distributed.

3.1.3. N_2 physisorption

The results obtained from the N_2 physisorption analysis are summarised in Table 2. The untreated alumina support has a BET surface area of 227.2 m^2/g, a BJH pore volume of 0.77 cm^3/g, and a median pore diameter of 12.2 nm. The metal-loaded fresh samples have a smaller surface area and pore volume compared to the bare support, as the metal particles may block the pores of alumina during the impregnation process [24]. The surface area, pore volume, and pore size were slightly increased after the reduction process, apart from Ni_3Ge_1, which showed a slightly decreased surface area. This stems from the formation of large binary NiGe crystallites upon reduction at higher temperatures (800 °C) [10]. As shown in Table 3, Ni_3Ge_1 had the largest crystallite size and therefore, fewer exposed surfaces compared to smaller crystallites. The BJH analysis indicated that the catalysts are mesoporous, with median pore diameters in the range of 10–14 and 12–15 nm for the fresh and reduced samples, respectively. Among the bimetallic catalysts, Ni_3Cu_1/Al_2O_3 showed a higher surface area compared with the monometallic Ni catalyst. This promoting effect of Cu on the overall textural properties of the bimetallic catalyst was also observed by Khzouz et al. [7], and is attributed to the more uniform distribution of the metallic species on the support surface and less blockage of pores.

3.1.4. H_2 chemisorption

The hydrogen uptake amount, metal dispersion rate, metallic surface area, and crystallite size of the catalysts obtained by H_2 chemisorption analysis are summarized in Table 3. The highest H_2 uptake amount was obtained by Ni/Al_2O_3 with a metal dispersion rate of 1.07 %, which is on a similar level as other alumina-supported Ni catalysts synthesized by the wet-impregnation method [25]. Compared with Ni/Al_2O_3, all bimetallic catalysts showed a lower H_2 uptake amount. The dilution of surface Ni atoms by the addition of the second element and the formation of bimetallic alloys (as evidenced by the XRD results in section 3.1.5) decreased the H_2 uptake amount and the metallic surface area of Ni. This is consistent with the results reported in previous literature, where the dispersion rate of the main active metal is decreased when Cu [26], Fe [27] or Ge [28] is added. It is also observed that the addition of Cu and Fe decreased the crystallite size of the bimetallic catalysts, whereas Ge significantly increased it.

3.1.5. XRD analysis

The XRD patterns of the reduced samples with a zoom of the peaks in the range of 40°–55° are presented in Fig. 3, and the peaks were fitted using the Inorganic Crystal Structure Database [29]. No crystallite peaks were detected for the bare alumina support, indicating that the alumina used was amorphous, which is not unexpected [30,31]. In Fig. 3 (b), the

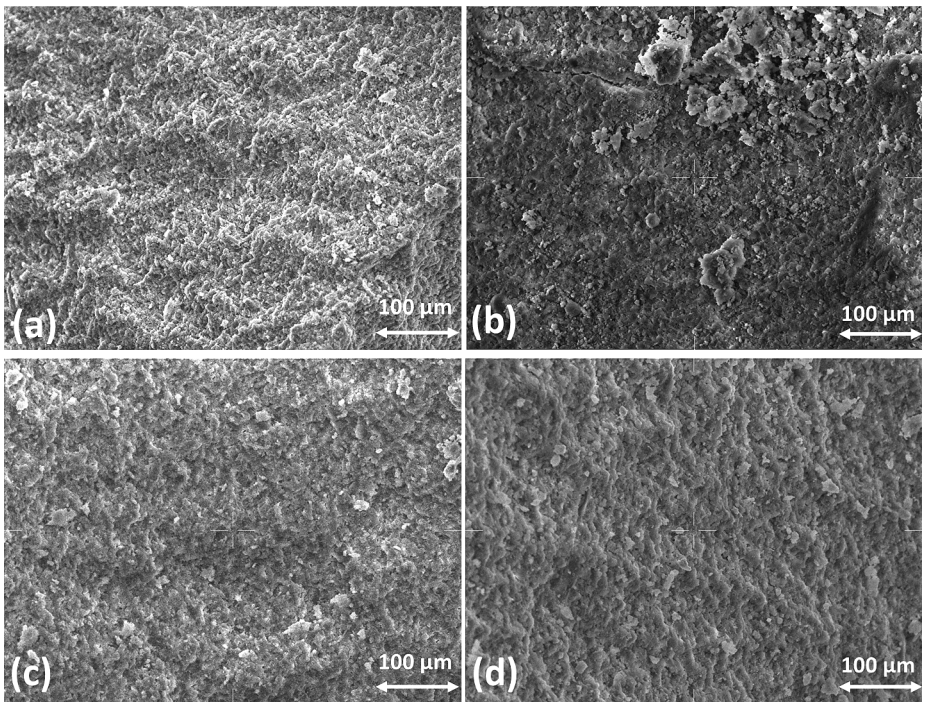

Fig. 1. SEM images of (a) Ni/Al_2O_3, (b) Ni_3Cu_1/Al_2O_3, (c) Ni_3Fe_1/Al_2O_3, (d) Ni_3Ge_1/Al_2O_3.

dashed lines indicate the positions of the (1 1 1) and (2 0 0) reflections of pure Ni. The peaks with the highest intensity located at 44.25°, 44.21°, and 43.53° were assigned to the (1 1 1) peaks of the Ni_3Cu_1, Ni_3Fe_1, and Ni_3Ge_1 solid solutions, respectively. The peaks with lower intensity between 50°–52° and 74°–76° correspond to the (2 0 0) and (2 2 0) surfaces of the face centred cubic bimetallic alloys. The shift of the peaks to lower angles compared with pure Ni confirmed the formation of bimetallic alloys and also indicates an increase in the lattice size of the alloys compared with pure Ni [32]. The lattice constant of Ni_3Cu_1, Ni_3Fe_1, and Ni_3Ge_1 were estimated using Bragg's Law and were calculated to be 3.538, 3.541, and 3.577 Å, respectively. No other peaks with low intensities were identified, showing the high crystallinity and phase purity of the alloy formed after the reduction process [33].

3.1.6. XPS analysis

The surface state of the reduced samples was examined using XPS analysis, and the spectra obtained are presented in Fig. 4. In Fig. 4 (a), the 2p 3/2 peaks at 852.6 and 856.2 eV are attributed to metallic Ni^0 and NiO (Ni^{2+}), respectively. The 2p 1/2 peak at 873.6 eV was attributed to NiO (Ni^{2+}). Weaker satellite peaks were observed at the higher binding energy side of the two main peaks (861.8 and 880.6 eV), which is a typical characteristic of nickel [34]. The same main peaks and their corresponding satellite peaks were also observed for two of the bimetallic catalysts (Fig. 4 (b) and (c)). However, the peaks are slightly shifted towards to higher binding energy side, which is possibly due to their strong interaction with the alumina support [32]. For Ni_3Ge_1/Al_2O_3, the peaks at 854.1 and 871.7 eV are attributed to $Ni(OH)_2$ (Ni^{2+}). The presence of nickel oxide and hydroxide species in the samples is due to the passivation layers formed on the surface of the fine Ni particles at room temperature [35,36]. In the Cu 2p spectrum, the peaks at 934.4 and 954 eV correspond to CuO (Cu^{2+}) 2p 3/2 and Cu^0 2p ½, respectively [37,38]. The Fe 2p spectrum contains three main peaks with relatively low intensity at 707, 711.5, and 724.8 eV, which correspond to Fe^0 2p 3/2, a combination of Fe^{2+} 2p 3/2 and Fe^{3+} 2p 3/2, and a combination of Fe^{2+} 2p 1/2 and Fe^{3+} 2p 1/2 [39,40]. Similar to Ni, the passivation of copper and iron can occur under ambient temperature when exposed to air [41,42], which explains the presence of the oxide species in the samples. Finally, two peaks at 1222 and 1253 eV were observed in the Ge 2p spectrum, corresponding to GeO_2 (Ge^{4+}) 2p 3/2 and GeO_2 (Ge^{4+}) 2p 1/2 [43]. Similarly, this was possibly due to the inevitable oxidation by air during storage and transportation of the samples. A thin layer of GeO_2 usually forms on the surface of Ge, which can take place even at room temperature when exposed to air [44].

3.2. Catalytic performance study for steam methane reforming

The catalytic performance of Ni/Al_2O_3 and the bimetallic catalysts for the SMR reaction was evaluated based on the CH_4 conversion, H_2 yield, and purity, as well as the CO selectivity. To evaluate the repeatability of the experiments, SMR tests using Ni_3Cu_1/Al_2O_3 were repeated three times at 600, 700, and 800 °C, and the standard deviation error bars of each set of results were plotted in Fig. 5.

All catalysts showed an increase in methane conversion with higher reaction temperature, as the SMR reaction is endothermic. It was also found that for Ni, Ni_3Cu_1, and Ni_3Ge_1, the gap between the observed catalytic activity and the equilibrium gradually reduced as reaction temperature increased. The reaction at 600 °C was potentially due to diffusion limitations. Xu and Froment [45] proposed that intraparticle diffusion can be neglected for catalyst particles which are smaller than 0.2 mm. The diameter of the catalysts used in this work was approximately 3 mm. Based on the study by Pashchenko [46], a particle size of 3 mm significantly affects the diffusion within the catalyst particle, with an effectiveness factor (effectiveness factor = $\frac{\text{reaction rate with diffusion limitation}}{\text{reaction rate withour diffusion limitation (intrinsic kinetic)}}$) of 0.03. This explains the difference between the observed value at 600 °C and equilibrium. As the reaction temperature gradually increased, the reaction rate of the SMR and WGS reactions increased and the activity of the catalysts approached the thermodynamic equilibrium.

The promoting effect of Ge and Cu becomes increasingly significant as reaction temperature rises, with the highest methane conversion of 87 % achieved by Ni_3Cu_1/Al_2O_3 at 800 °C. The difference between the methane conversion level at thermodynamic equilibrium and the measured values is potentially due to the high GHSV (15,000 h^{-1}) used and the low methane concentration (10 vol%) in the feed stream, which decreased the possibility of contact between the reaction gases and the

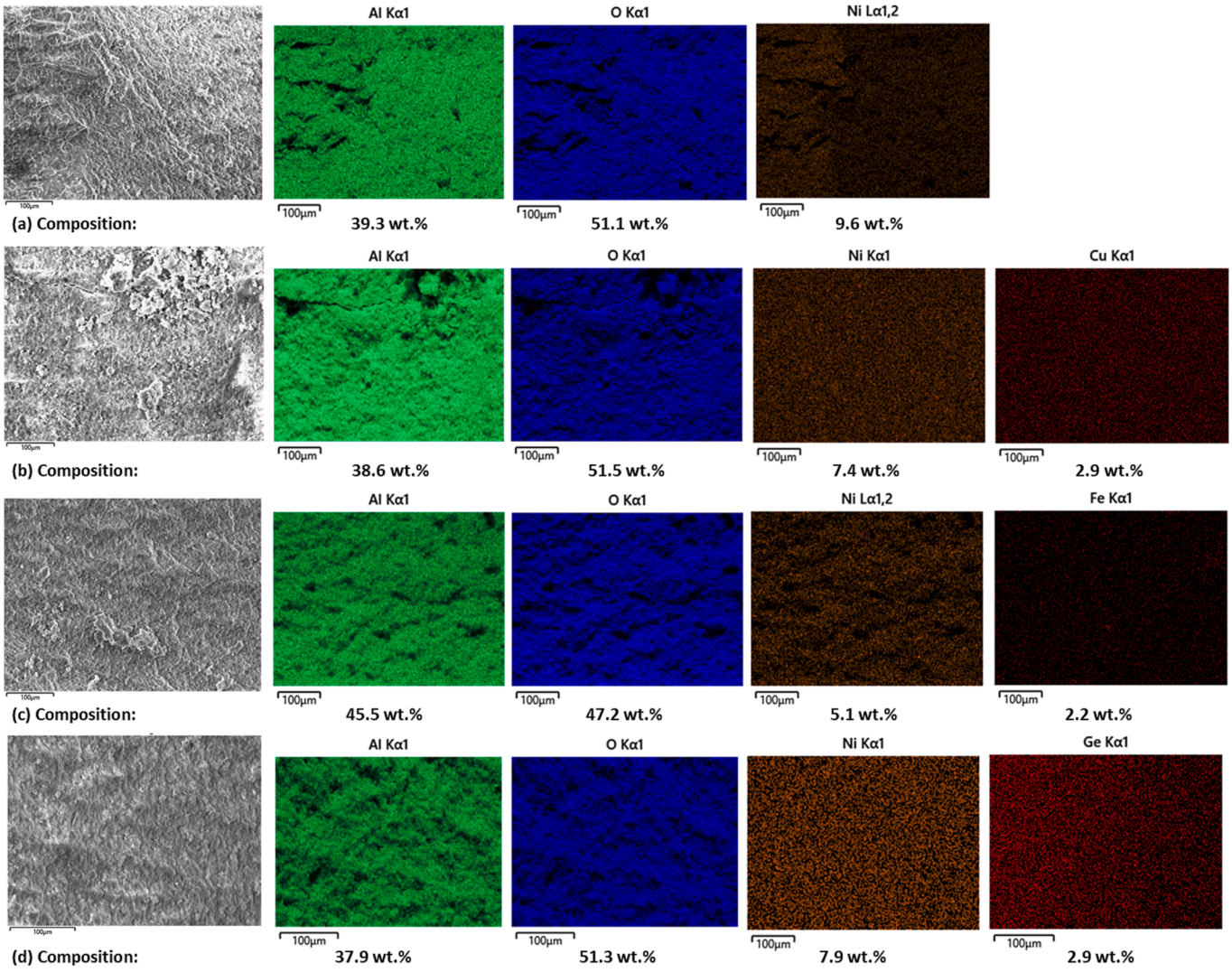

Fig. 2. EDX elemental mapping of (a) Ni/Al_2O_3, (b) Ni_3Cu_1/Al_2O_3, (c) Ni_3Fe_1/Al_2O_3, (d) Ni_3Ge_1/Al_2O_3.

Table 2
Results from N_2 physisorption analysis.

	BET surface area (m^2/g)		BJH adsorption pore volume (cm^3/g)		BJH adsorption median pore diameter (nm)	
Alumina	227.16		0.77		12.22	
	Fresh	Reduced	Fresh	Reduced	Fresh	Reduced
Ni/Al_2O_3	190.3	227.7	0.62	0.77	11.96	12.37
Ni_3Cu_1/Al_2O_3	217.0	222.5	0.69	0.77	11.50	12.56
Ni_3Fe_1/Al_2O_3	176.3	180.7	0.62	0.70	13.35	14.30
Ni_3Ge_1/Al_2O_3	179.5	159.6	0.52	0.58	10.84	13.61

Table 3
Results from H_2 pulse chemisorption tests.

	H_2 uptake (μmol/g)	Metal dispersion (%)	Metallic surface area		Crystallite size (Å)
			m^2/g sample	m^2/g metal	
Ni/Al_2O_3	14.04	1.07	0.56	5.56	1,010.3
Ni_3Cu_1/Al_2O_3	9.43	1.56	0.37	5.33	505.4
Ni_3Fe_1/Al_2O_3	8.14	0.62	0.41	4.07	410.4
Ni_3Ge_1/Al_2O_3	5.21	0.42	0.25	2.48	2,940.5

catalyst. Similar to Cu, Ge enhanced the catalytic activity of Ni catalyst at 800 °C with a methane conversion rate of 80 %. A similar trend was observed for hydrogen yield and hydrogen purity – both values increase as temperature rises. Compared with the monometallic Ni catalyst, Ni_3Cu_1/Al_2O_3 and Ni_3Ge_1/Al_2O_3 showed higher hydrogen yield and purity at higher temperatures, with a maximum value of 64 % and 72 %, respectively.

It is generally agreed that noble metals are the most active for SMR – Ru-, Rh-, Pt-, and Pd-promoted Ni catalysts were reported to be able to achieve a methane conversion same to the thermodynamic equilibrium level [47–49]. Although the methane conversion of Ni_3Cu_1/Al_2O_3 and Ni_3Ge_1/Al_2O_3 are 10–15 % lower compared with the noble metal-promoted catalysts, it should be noted that Cu and Ge are much more available and cost-effective.

CO selectivity serves as a measurement of the extent of the WGS reaction within the system. As demonstrated by Eq. (2), the WGS reaction allows for the production of more hydrogen through the conversion of CO and H_2O. As shown in Fig. 5 (d), the CO selectivity of Ni_3Cu_1/Al_2O_3 and Ni_3Ge_1/Al_2O_3 was on a similar or lower level compared with Ni/Al_2O_3. In particular, both Ni_3Cu_1/Al_2O_3 and Ni_3Ge_1/Al_2O_3 showed a higher methane conversion rate with a lower CO selectivity at 800 °C.

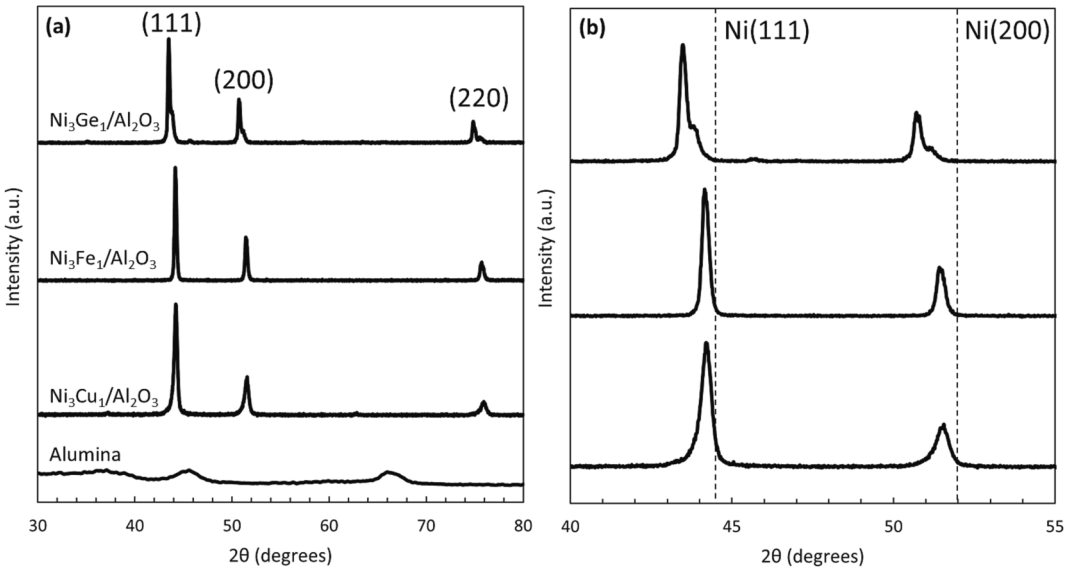

Fig. 3. XRD patterns of the alumina support and the reduced bimetallic catalysts: (a) overall pattern (b) a zoom of the 2θ range of 40°–55°.

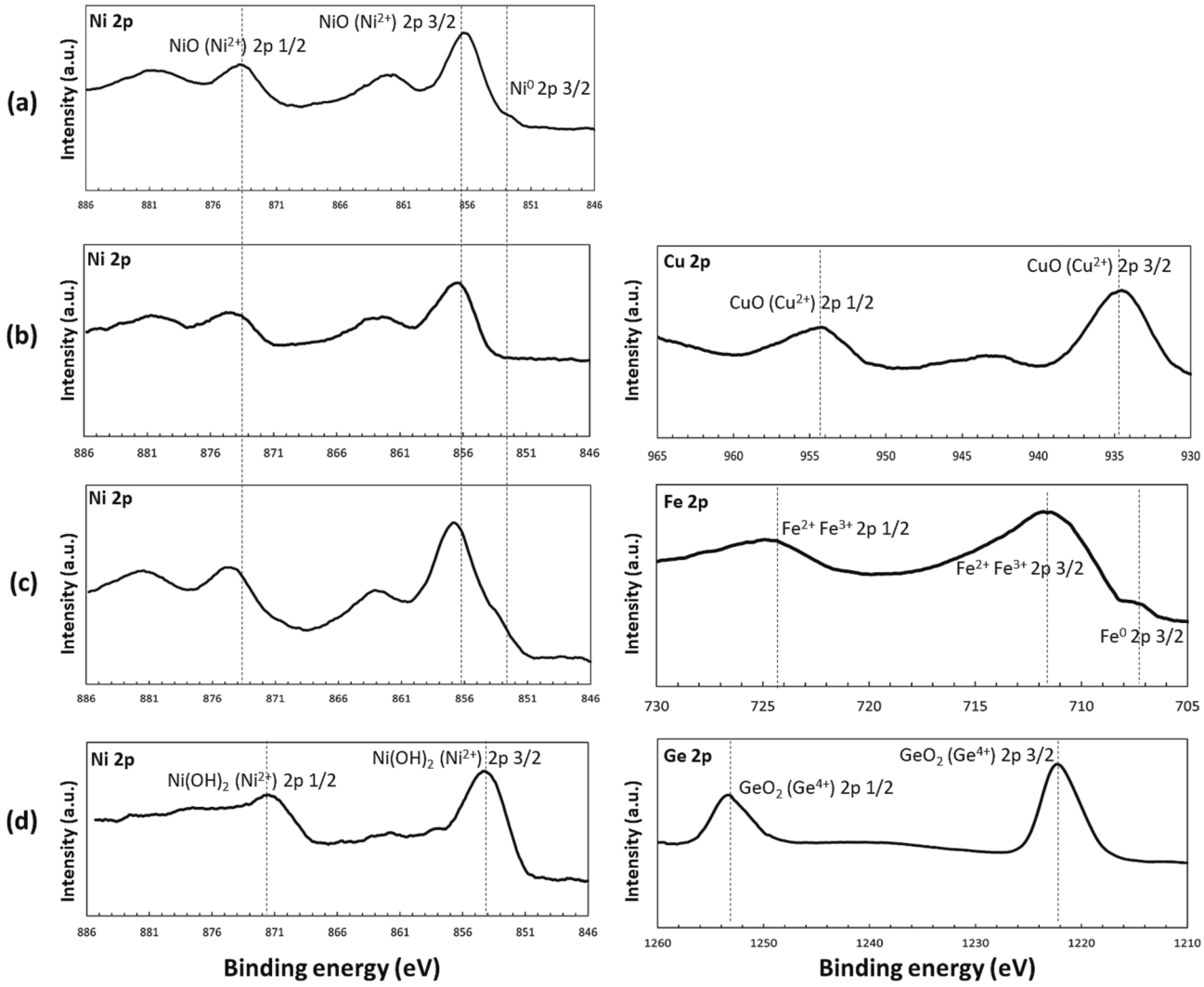

Fig. 4. XPS spectra of reduced (a) Ni/Al_2O_3, (b) Ni_3Cu_1/Al_2O_3, (c) Ni_3Fe_1/Al_2O_3, (d) Ni_3Ge_1/Al_2O_3.

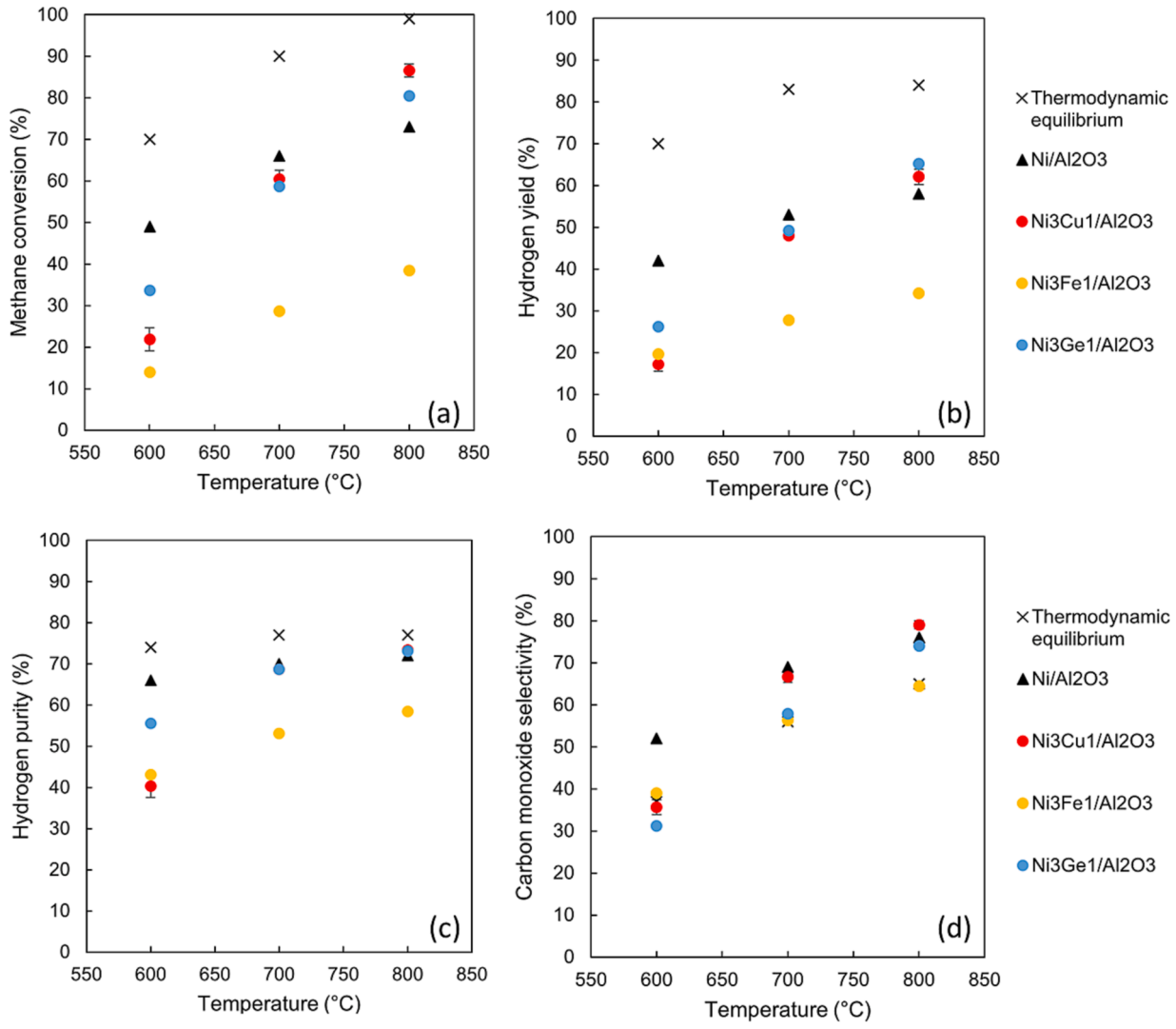

Fig. 5. (a) Methane conversion, (b) hydrogen yield, (c) hydrogen purity, and (d) CO selectivity of the mono and bimetallic catalysts under SMR conditions.

This indicates that the addition of Cu and Ge improved the activity of the catalysts by enhancing the WGS reaction, the methane consumed by the SMR reaction was therefore further converted to CO_2 through WGS, leading to a low CO selectivity.

The theoretical H_2 purity was found to be maintained at a relatively stable level from 600 to 800 °C with a slight increase as temperature rises. However, it is observed in Fig. 5 (c) that there is a significant increase in H_2 purity from 600 to 700 °C. At 600 °C, the reactions using all four catalysts were far from reaching the thermodynamic equilibrium, leading to a large difference in the concentration of CH_4 and H_2 at the outlet (CH_4 out and H_2 out) compared to the theoretical value. As the reaction temperature increased to 700 °C and the reaction gradually approached equilibrium, the gap between the theoretical and observed CH_4 out and H_2 out values reduced. The trend in H_2 purity at higher temperatures therefore resembles the theoretical trend more at 700 and 800 °C, compared with at 600 °C.

On the other hand, the addition of Fe has a significant negative impact on the activity of the catalyst, which is in contraction to the predictive results reported by Xu et al. [5]. This is partially due to the morphological properties of Ni_3Fe_1/Al_2O_3 – as shown by both XRF and SEM-EDX analysis, Fe particles tend to segregate on the surface of the alumina support, which may lead to blockage of surface pores, leaving insufficient entrance for reactant gases to enter the support. Ni-Fe alloy also requires a relatively high reduction temperature, which is between 600 and 800 °C based on previous literature [50,51]. This may have led to incomplete activation of the Ni_3Fe_1/Al_2O_3 catalyst prior to the SMR test, as results from the XPS analysis evidenced the presence of iron oxide species within the reduced sample. To further explore how the addition of Cu, Fe, and Ge influences the performance of the nickel catalyst, a series of first principle-based calculations and microkinetic modelling were carried out, and the results are presented in section 3.4.

The used catalysts were characterized using N_2 physisorption and TGA, and the results are summarized in Table 4. The amount of carbon presented in the table is the accumulated amount after three consecutive

Table 4
Properties of the used catalysts after SMR tests.

	BET surface area (m^2/g)	BJH adsorption pore volume (cm^3/g)	BJH adsorption median pore diameter (nm)	Accumulated carbon amount (wt.%)
Ni/Al_2O_3	180.9	0.65	12.37	3.37
Ni_3Cu_1/Al_2O_3	192.4	0.76	14.46	2.26
Ni_3Fe_1/Al_2O_3	164.7	0.65	14.74	2.98
Ni_3Ge_1/Al_2O_3	163.7	0.58	13.62	3.29

SMR tests, with reaction temperature varying from 600 to 800 °C. Once subjected to the approximately 1.5-hour SMR test, the surface area and pore volume of the catalysts were decreased with an increase in pore diameter. This is as expected, due to the potential sintering of the active metals and pore blockage by coke at higher temperatures. All bimetallic catalysts showed a better carbon resistant ability compared with the monometallic Ni/Al_2O_3, with the lowest carbon formation amount of 2.26 % achieved by Ni_3Cu_1/Al_2O_3. The enhanced stability of the bimetallic catalysts may be achieved due to the formation of Ni-based alloys (as indicated by the XRD results in section 3.1.5.), which prevented the formation of bulk Ni particles prone to coke formation [9]. The low carbon deposition amount was also attributed to the reaction conditions employed. It has been found that for SMR reaction at equilibrium under atmospheric pressure with a steam-to-carbon ratio of 3, no carbon formation was observed when the reaction temperature exceeded 700 °C [52]. It was also observed that for short-term tests (<2h), a reaction temperature of 800 °C significantly suppressed carbon formation compared to 600 °C [52]. It is therefore concluded that a reaction temperature of 800 °C is optimal for the SMR process, as the bimetallic catalysts are able to reach their highest activity with minimal carbon deposition amount.

3.3. Catalytic performance study for sorption-enhanced steam methane reforming

The catalytic performance of Ni/Al_2O_3 and the bimetallic catalysts was also evaluated under SESMR conditions at 600, 650, and 700 °C, and the results are presented in Fig. 6. Fig. 7 presents the composition of the outlet gas stream of the SESMR test at 700 °C using Ni/Al_2O_3 as the catalyst.

By increasing the reaction temperature from 600 to 700 °C, both methane conversion and hydrogen yield were improved. This was attributed to the enhancement of the endothermic SMR reaction (Eq. (1)), while in the meantime, the adverse effect of high temperature on the exothermic WGS and CO_2 adsorption reactions (Eq. (2) and (3)) was not as significant. Compared with the SMR test under the same reaction temperature (T = 700 °C), the addition of the CO_2 sorbent improved the methane conversion of all catalysts by approximately 20–30 %. The highest methane conversion rate of 95 % was achieved by Ni/Al_2O_3 and Ni_3Cu_1/Al_2O_3 at 700 °C. Similarly, hydrogen yield, hydrogen purity, and CO selectivity were all enhanced in the presence of the sorbent. The sorbent in the system effectively absorbs the CO_2 produced through the WGS reaction and therefore moves the reaction equilibrium towards the direction of hydrogen production. The concentration of CO_2 in the outlet gas stream at 700 °C was approximately 2 vol% (corresponding to a CO selectivity of ~73 %). The outlet CO_2 concentration can be further decreased by reducing the GHSV of the system to increase the contact time between CO_2 and the sorbent, or by reducing the particle size of the sorbent [53]. However, it should be noted that CO_2 absorption by calcium oxide is exothermic (Eq. (3)), a further increase in temperature beyond 700 °C will result in the process returning to its conventional SMR state. It is concluded that for the bimetallic catalysts focused on in this study, 700 °C is the optimal temperature for the materials to achieve the best performance, in terms of highest methane conversion, hydrogen yield, and purity.

Compared with the tests under SMR conditions, the promoting effect of Ge is not as significant under SESMR conditions. Methane conversion, hydrogen yield, and hydrogen purity of Ni_3Ge_1/Al_2O_3 were found to be lower than the monometallic Ni/Al_2O_3. It is also observed that Ni_3Ge_1/Al_2O_3 exhibited the lowest CO selectivity, meaning that CO_2 has not been effectively absorbed in the system. TGA tests of used sorbent from the SESMR tests at 700 °C were carried out and the TGA curves are

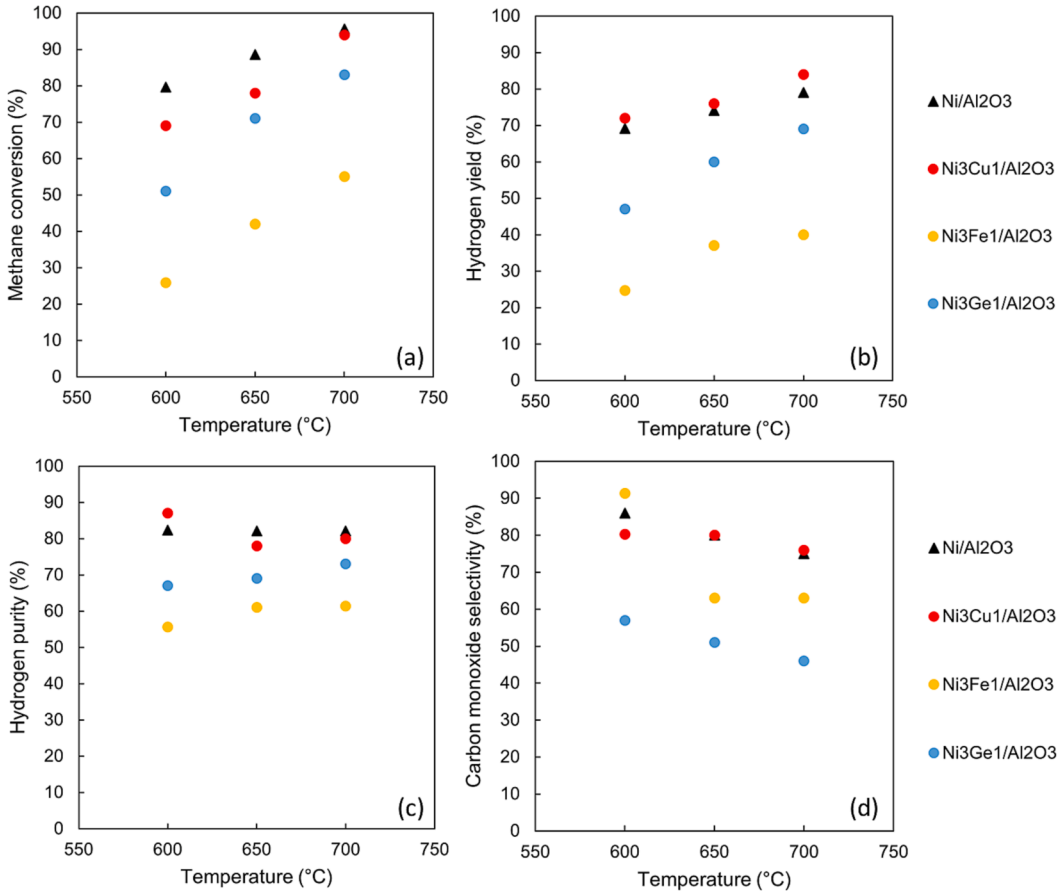

Fig. 6. (a) Methane conversion, (b) hydrogen yield, (c) hydrogen purity, and (d) CO selectivity of mono and bimetallic catalysts under SESMR conditions.

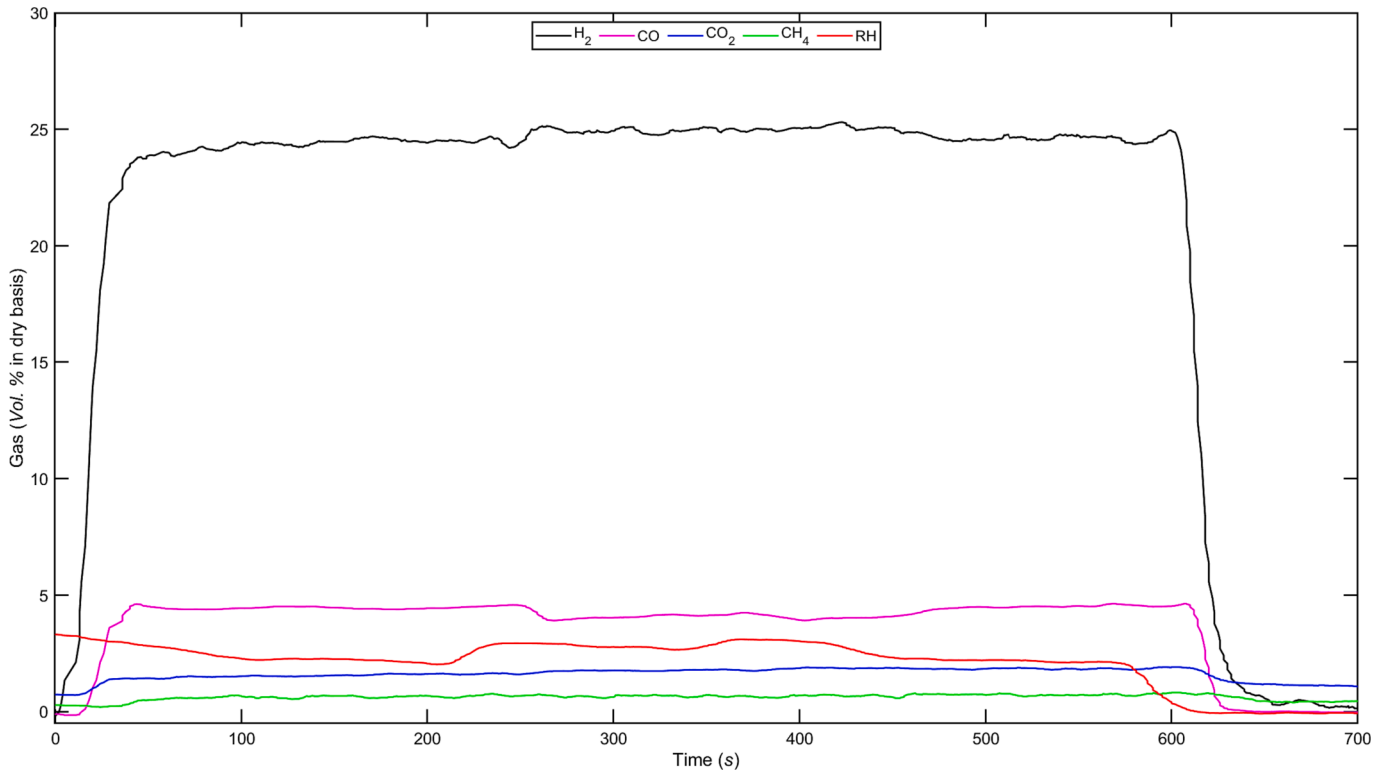

Fig. 7. Composition of the outlet gas stream for SESMR at 700 °C (using Ni/Al_2O_3 as catalyst).

shown in Fig. 8. The amount of carbon deposited on the used sorbent from the four tests was calculated to be 4.68 wt%, 6.07 wt%, 6.06 wt%, and 6.80 wt%, respectively (using Equation (7)). It was observed that the amount of deposited carbon for the three tests using bimetallic catalysts was higher than that observed in the test using monometallic Ni. This is potentially due to the high carbon resistance of the three bimetallic catalysts, as demonstrated in Table 4, making elemental carbon more likely to be deposited on the surface of the calcium oxide sorbent. The relatively low CO selectivity of Ni_3Ge_1/Al_2O_3 was therefore attributed to the highest carbon deposition amount on the sorbent surfaces during the reaction – although sufficient steam-to-carbon ratio was utilised for the reaction, a relatively large amount of carbon in the feed was converted into coke instead of CO through side reactions, such as methane cracking or the Boudouard reaction [54]. The carbon formed was deposited on the surface of the calcium oxide sorbent, reducing its ability to effectively absorb the CO_2 formed by the WGS reaction.

3.4. Microkinetic modelling of SMR and DFT calculations for the bimetallic systems

As mentioned in section 1, Ni_3Fe_1 was predicted to be one of the catalysts with the highest SMR activity. However, this is in contradiction to the results presented in this paper (section 3.2). In order to ascertain the cause of this difference between numerical and experimental results, and to further investigate the promoting effect of Cu and Ge in the bimetallic systems, a combined DFT and MKM study was conducted.

In the work by Xu et al. [5], DFT-calculated adsorption energies of carbon and oxygen on the (211) bimetallic surface were used to evaluate the catalytic activity of the materials, which are summarised in Table 5. However, based on results from the XRD analysis (section 3.1.5) and extensive literature data [55–58], only the (111), (200) and (220) phases are present in the reduced catalysts, among which (111) is the most dominant. The catalytic activity of the bimetallic catalysts involved in this study is therefore mainly determined by the atomic/molecular adsorption energies of the species involved in the SMR reaction on the (111) surface. It is therefore possible that the difference between the prediction and the experimental results is due to a difference in surface energetics. To confirm this, we have calculated the adsorption energies of carbon and oxygen on the Ni(111), Ni_3Cu_1(111), Ni_3Fe_1(111), and Ni_3Ge_1(111) surfaces as these values are not all readily available from pre-existing literature. As can be seen from Table 5, there is a 0.1–0.8 eV difference between the adsorption energies on the (111) and (211) surfaces. The (211) surface shows a stronger adsorptive ability towards carbon in general, whereas its oxygen adsorptive ability is weaker in the case of Ni_3Fe_1 and Ni_3Ge_1.

To evaluate how different adsorption energies affect the overall catalytic activity for the SMR reaction, the eight materials listed in Table 5 were plotted against a "volcano plot" (Fig. 9). The volcano plot was obtained from the microkinetic model developed using the approach described in the methodology section (section 2.5). The result shows the turnover frequency (TOF) of H_2 production as a function of the carbon and oxygen adsorption energies, which is a measurement of the material's catalytic activity for the SMR reaction.

The four (211) surfaces are indicated by the triangles on the volcano plot. Ni(211), Ni_3Fe_1(211), and Ni_3Ge_1(211) are located in the central region of the plot, indicating the highest TOF (10^{-3} s^{-1}), and therefore highest catalytic activity. This is consistent with the previous prediction that Ni_3Fe_1 and Ni_3Ge_1 are the most active bimetallic catalysts for SMR. However, if the prediction is to be made based on the (111) surfaces (indicated by the crosses on the volcano plot), it is evidenced that Ni_3Cu_1 is the most optimal with a TOF of 10^{-4} s^{-1}. Ni_3Ge_1 was also shown to be an active catalyst with the second highest H_2 TOF. On the other hand, compared with Ni_3Fe_1(211), its (111) surface has significantly lower carbon and oxygen adsorption energies, leading to a relatively lower catalytic activity. Based on the (111) surfaces, the relative activity of the mono and bimetallic catalysts was found to be $Ni \approx Ni_3Cu_1 > Ni_3Ge_1 > Ni_3Fe_1$, which is consistent with the results obtained from the experimental testing. It is concluded that the low catalytic activity of Ni_3Fe_1/Al_2O_3 is due to a combination of different factors – including both physical and chemical properties. As indicated by the XRF and SEM-EDX

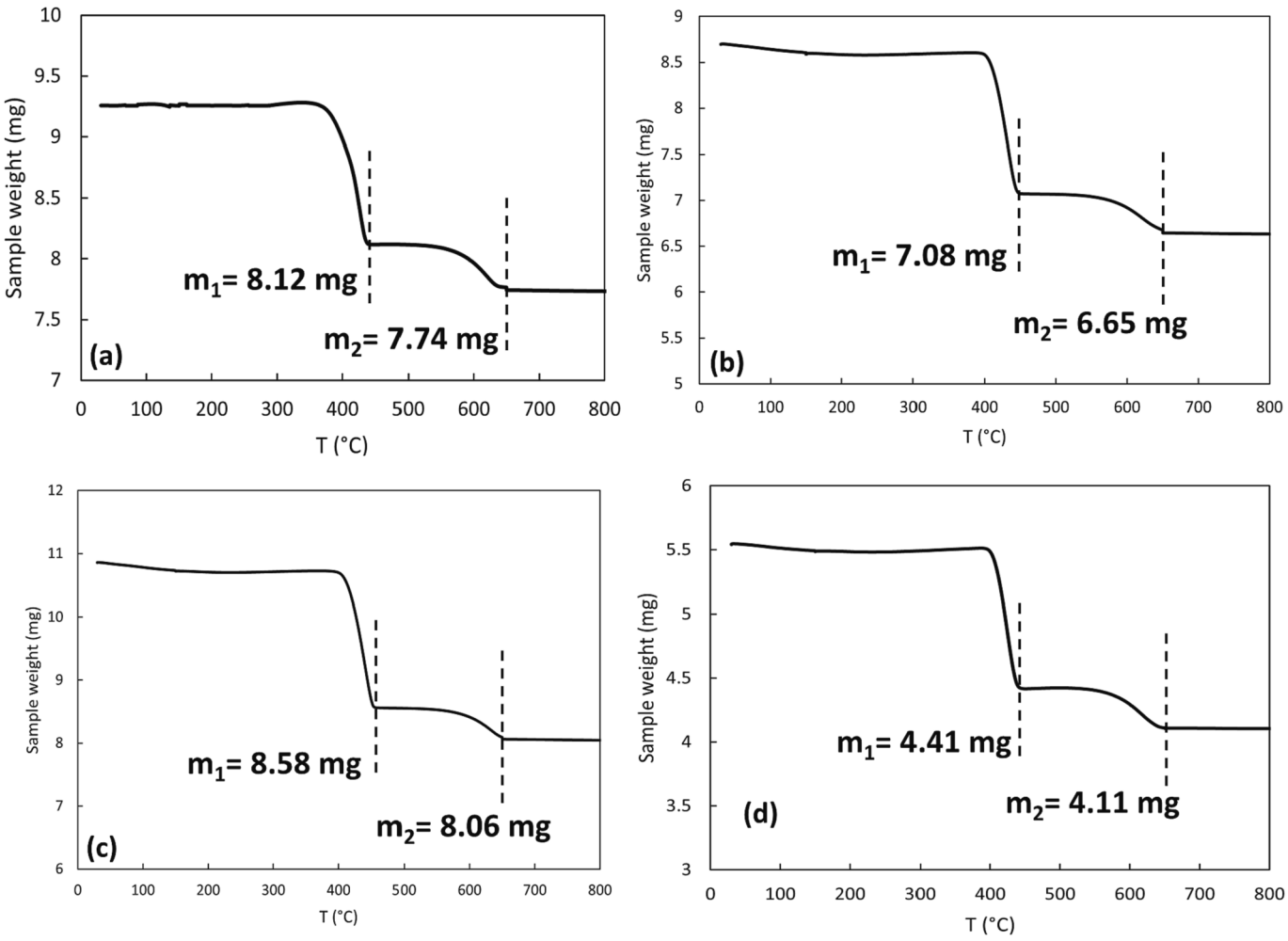

Fig. 8. TGA curves of the used sorbent from the SESMR tests using (a) Ni/Al_2O_3, (b) Ni_3Cu_1/Al_2O_3, (c) Ni_3Fe_1/Al_2O_3, and (d) Ni_3Ge_1/Al_2O_3 as catalysts.

Table 5
Adsorption energies on the (1 1 1) surface (obtained by DFT calculations) and on the (2 1 1) surface (extracted from literature [5,64]).

Surface	C adsorption energy (eV)	O adsorption energy (eV)	Surface	C adsorption energy (eV)	O adsorption energy (eV)
Ni(1 1 1)	−7.9	−5.4	Ni(2 1 1)	−8.2	−5.5
Ni_3Cu_1(1 1 1)	−7.8	−5.3	Ni_3Cu_1(2 1 1)	−8.6	−5.6
Ni_3Fe_1(1 1 1)	−8.9	−6.4	Ni_3Fe_1(2 1 1)	−8.3	−5.7
Ni_3Ge_1(1 1 1)	−7.3	−5.9	Ni_3Ge_1(2 1 1)	−8.4	−5.5

analysis (sections 3.1.1 and 3.1.2), Fe tends to segregate on the outer surface of the alumina support, making it difficult for the reactant gases to diffuse to the active sites located inside the support. Another negative impact of Fe addition is on the reducibility of the catalysts. Temperature Programmed Reduction studies on bimetallic Ni-Fe catalysts [59–61] have shown that the addition of Fe shifted the reduction peak to a higher temperature, compared to the monometallic Ni catalyst. This increased the difficulty of fully activating the bimetallic Ni-Fe catalyst before each performance testing, leading to lower catalytic activity. Finally, the most important reason for the lower activity of Ni_3Fe_1/Al_2O_3 was attributed to its undesirably high adsorption ability towards carbon and oxygen. Based on the Sabatier Principle [62,63], the best-performing catalyst should bind the atoms/molecules involved in the reaction with an intermediate strength – not too weak so that reactions can be activated, and not too strong so that the products can detach from the catalyst surface. In the case of this study, the optimal binding strength for the SMR reaction was estimated to be between −8.5 and −7.0 eV for carbon, and between −6.0 and −5.0 eV for oxygen (based on the central region coloured in red in Fig. 9). The adsorption strength of Ni_3Fe_1 towards carbon and oxygen is too strong (i.e. the adsorption energies are too low), making it therefore unsuitable for the SMR reaction.

The DFT calculations on both (2 1 1) and (1 1 1) surfaces also indicate that the crystallite phase of a given catalyst can significantly influence its catalytic activity. The overall performance of the catalyst is therefore also dependent upon the synthesis method employed during the experiments, and the amount of (1 1 1) surface produced in the synthesized samples.

It is also generally acknowledged that the method used for the DFT calculations (e.g., functionals, pseudopotentials, etc) can affect the final results obtained. It is therefore of interest that a systematic database be built for molecular and atomic adsorption on the (1 1 1) phase of transition metals and alloys, as it is usually the most exposed and close-packed surface in transition metal-based species. This will greatly facilitate the accurate prediction of catalytic activity for SMR and other reactions alike.

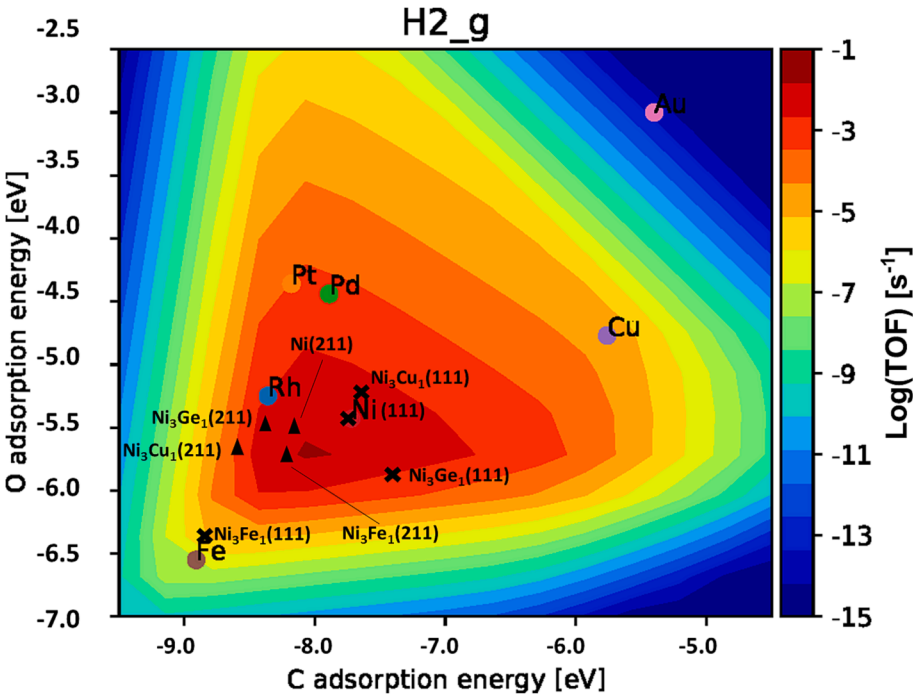

Fig. 9. TOF of H_2 production as a function of carbon and oxygen adsorption energies.

4. Conclusions

Three bimetallic catalysts have been successfully synthesized using the wet impregnation method, and the formation of Ni-Cu, Ni-Fe, and Ni-Ge bimetallic solid solutions upon reduction was confirmed by XRD analysis. XRF and EDX analysis showed that Ni, Cu, and Ge were homogeneously distributed within the porous alumina support, whereas Fe tended to segregate on the outer layer of the support. The addition of Cu improved the overall surface area and metal dispersion rate compared to the monometallic Ni catalyst, whereas a slight decrease was observed for Fe and Ge. The optimal physical and chemical properties of the Ni_3Cu_1/Al_2O_3 catalyst were also reflected in its catalytic performance. The highest methane conversion of 87 % for SMR tests was achieved by Ni_3Cu_1/Al_2O_3 at 800 °C under high GHSV conditions, proving it to be a promising low-cost alternative to conventional Ni catalysts and noble metal-based catalysts. Similarly, the addition of Ge improved the overall activity of the monometallic Ni catalyst, and the effect is most significant at high temperatures. The bimetallic Ni-Fe catalyst on the other hand, showed a lower activity compared to Ni. The experimental observations were also supported by ab-initio DFT calculations and microkinetic modelling. DFT calculations of molecular and atomic adsorption energies were carried out for the (1 1 1) and (2 1 1) surfaces of the mono and bimetallic materials, and a clear difference in their carbon and oxygen adsorption abilities was observed. This explained the inconsistency between the experimental results and the conclusions made based on previous numerical screening processes. The microkinetic model indicated that both Ni_3Ge_1(1 1 1) and Ni_3Cu_1(1 1 1) were able to achieve a similar level of hydrogen production rate as Ni(1 1 1), whereas the Ni_3Fe_1(1 1 1) surface is not suitable for the SMR reaction. TGA tests of the used catalysts showed that the carbon-resistant ability of the catalysts was enhanced by the formation of bimetallic alloys. However, further study is needed to investigate the stability of the materials under long-term SMR conditions. It would also be of interest to carry out more advanced characterization tests on the bimetallic catalysts, including Transmission Electron Microscopy, to obtain information on the inner structure of the catalyst, and the distribution, size, and shape of the alloy particles formed. The addition of calcium oxide as the CO_2 sorbent enhanced the overall performance of all materials, with Ni/Al_2O_3 and Ni_3Cu_1/Al_2O_3 reaching a methane conversion of 97 % at 700 °C, which is close to the thermodynamic equilibrium level. Hydrogen yield and hydrogen purity were also improved by 30 % and 20 % respectively, proving SESMR to be a promising technology for low-carbon hydrogen production. In conclusion, this combined experimental and numerical investigation of bimetallic catalysts has identified promising novel materials for the application of (SE)SMR and provided directions for future research in this field.

Funding

This research did not receive any specific grant from funding agencies in the public, commercial, or not-for-profit sectors.

CRediT authorship contribution statement

Siqi Wang: Investigation, Writing – original draft. **Ziqi Shen:** Investigation, Writing – original draft, Writing – review & editing. **Amin Osatiashtiani:** Resources. **Seyed Ali Nabavi:** Writing – review & editing. **Peter T. Clough:** Writing – review & editing, Supervision.

Declaration of competing interest

The authors declare that they have no known competing financial interests or personal relationships that could have appeared to influence the work reported in this paper.

Data availability

Data is available in Supplementary Information.

Appendix A. Supplementary data

Supplementary data to this article can be found online at https://doi.org/10.1016/j.cej.2024.150170.

References

[1] H. Zhang, Z. Sun, Y.H. Hu, Steam reforming of methane: current states of catalyst design and process upgrading, Renew. Sustain. Energy Rev. 149 (2021), https://doi.org/10.1016/j.rser.2021.111330.

[2] R. Soltani, M.A. Rosen, I. Dincer, Assessment of CO2 capture options from various points in steam methane reforming for hydrogen production, Int. J. Hydrogen Energy 39 (2014) 20266–20275, https://doi.org/10.1016/j.ijhydene.2014.09.161.

[3] S. Masoudi Soltani, A. Lahiri, H. Bahzad, P. Clough, M. Gorbounov, Y. Yan, Sorption-enhanced steam methane reforming for combined CO2 capture and hydrogen production: a state-of-the-art review, Carbon Capture Sci. Technol. 1 (2021), https://doi.org/10.1016/j.ccst.2021.100003.

[4] A. Boretti, B.K. Banik, Advances in hydrogen production from natural gas reforming, Adv. Energy Sustain. Res. 2 (2021), https://doi.org/10.1002/aesr.202100097.

[5] Y. Xu, A.C. Lausche, S. Wang, T.S. Khan, F. Abild-Pedersen, F. Studt, et al., In silico search for novel methane steam reforming catalysts, New J. Phys. 15 (2013), https://doi.org/10.1088/1367-2630/15/12/125021.

[6] Z. Liu, W. Tian, Z. Cui, B. Liu, A universal microkinetic-machine learning bimetallic catalyst screening method for steam methane reforming, Sep. Purif. Technol. 311 (2023), https://doi.org/10.1016/j.seppur.2023.123270.

[7] M. Khzouz, J. Wood, B. Pollet, W. Bujalski, Characterization and activity test of commercial Ni/Al2O 3, Cu/ZnO/Al2O3 and prepared Ni-Cu/Al 2O3 catalysts for hydrogen production from methane and methanol fuels, Int. J. Hydrogen Energy 38 (2013) 1664–1675, https://doi.org/10.1016/j.ijhydene.2012.07.026.

[8] T.J. Huang, S.Y. Jhao, Ni-Cu/samaria-doped ceria catalysts for steam reforming of methane in the presence of carbon dioxide, Appl. Catal. A 302 (2006) 325–332, https://doi.org/10.1016/j.apcata.2006.02.027.

[9] A. Djaidja, H. Messaoudi, D. Kaddeche, A. Barama, Study of Ni–M/MgO and Ni–M–Mg/Al (M=Fe or Cu) catalysts in the CH4–CO2 and CH4–H2O reforming, Int. J. Hydrogen Energy 40 (2015) 4989–4995, https://doi.org/10.1016/j.ijhydene.2014.12.106.

[10] S. Furukawa, G. Nishimura, T. Takayama, T. Komatsu, Highly active Ni- and Co-based bimetallic catalysts for hydrogen production from ammonia-borane, Front. Chem. 7 (2019), https://doi.org/10.3389/fchem.2019.00138.

[11] Garetto TF, Borgna A, Apesteguía CR. Effect of alloying on the sulfur resistance of bimetallic Pt-based catalysts, 1994, p. 369–76. https://doi.org/10.1016/S0167-2991(08)62762-7.

[12] H. Cui, S.Q. Turn, M.A. Reese, Removal of sulfur compounds from utility pipelined synthetic natural gas using modified activated carbons, Catal. Today 139 (2009) 274–279, https://doi.org/10.1016/j.cattod.2008.03.024.

[13] P. Frontera, P.L. Antonucci, A. Macario, Focus on materials for sulfur-resistant catalysts in the reforming of biofuels, Catalysts 11 (2021) 1029, https://doi.org/10.3390/catal11091029.

[14] S.A. Ghungrud, K.D. Dewoolkar, P.D. Vaidya, Cerium-promoted bi-functional hybrid materials made of Ni, Co and hydrotalcite for sorption-enhanced steam methane reforming (SESMR), Int. J. Hydrogen Energy 44 (2019) 694–706, https://doi.org/10.1016/j.ijhydene.2018.11.002.

[15] K.D. Dewoolkar, P.D. Vaidya, Tailored Ce- and Zr-doped Ni/hydrotalcite materials for superior sorption-enhanced steam methane reforming, Int. J. Hydrogen Energy 42 (2017) 21762–21774, https://doi.org/10.1016/j.ijhydene.2017.06.235.

[16] L. Han, Q. Liu, Y. Zhang, Q. Wang, N. Rong, X. Liang, et al., Catalytic toluene reforming with in situ CO 2 capture via an iron-calcium hybrid absorbent for promoted hydrogen production, Energ. Technol. 8 (2020), https://doi.org/10.1002/ente.202000083.

[17] Z. Shen, S.A. Nabavi, P.T. Clough, Design and performance testing of a monolithic nickel-based SiC catalyst for steam methane reforming, Appl. Catal. A 119529 (2023), https://doi.org/10.1016/j.apcata.2023.119529.

[18] M. Ayesha, A.H. Khoja, F.A. Butt, U. Sikandar, A.H. Javed, S.R. Naqvi, et al., Sorption enhanced steam reforming of methane over waste-derived CaO promoted MgNiAl hydrotalcite catalyst for sustainable H2 production, J. Environ. Chem. Eng. 10 (2022) 107651, https://doi.org/10.1016/j.jece.2022.107651.

[19] P. Teixeira, C. Bacariza, P. Correia, C.I.C. Pinheiro, I. Cabrita, Hydrogen production with in situ CO2 capture at high and medium temperatures using solid sorbents, Energies (Basel) 15 (2022) 4039, https://doi.org/10.3390/en15114039.

[20] P. Giannozzi, S. Baroni, N. Bonini, M. Calandra, R. Car, C. Cavazzoni, et al., QUANTUM ESPRESSO: a modular and open-source software project for quantum simulations of materials, J. Phys. Condens. Matter 21 (2009) 395502, https://doi.org/10.1088/0953-8984/21/39/395502.

[21] P.E. Blöchl, Projector augmented-wave method, Phys. Rev. B 50 (1994) 17953–17979, https://doi.org/10.1103/PhysRevB.50.17953.

[22] J.P. Perdew, K. Burke, M. Ernzerhof, Generalized gradient approximation made simple, Phys. Rev. Lett. 77 (1996) 3865–3868, https://doi.org/10.1103/PhysRevLett.77.3865.

[23] A.J. Medford, C. Shi, M.J. Hoffmann, A.C. Lausche, S.R. Fitzgibbon, T. Bligaard, et al., CatMAP: a software package for descriptor-based microkinetic mapping of catalytic trends, Catal Letters 145 (2015) 794–807, https://doi.org/10.1007/s10562-015-1495-6.

[24] A. Chatla, M.M. Ghouri, O.W. El Hassan, N. Mohamed, A.V. Prakash, N.O. Elbashir, An experimental and first principles DFT investigation on the effect of cu addition to Ni/Al2O3 catalyst for the dry reforming of methane, Appl. Catal. A 602 (2020), https://doi.org/10.1016/j.apcata.2020.117699.

[25] M. Khzouz, J. Wood, K. Kendall, W. Bujalski, Characterization of Ni-Cu-based catalysts for multi-fuel steam reformer, Int. J. Low-Carbon Technol. 7 (2012) 55–59, https://doi.org/10.1093/ijlct/ctr019.

[26] B.C. Miranda, R.J. Chimentão, J. Szanyi, A.H. Braga, J.B.O. Santos, F. Gispert-Guirado, et al., Influence of copper on nickel-based catalysts in the conversion of glycerol, Appl. Catal. B 166–167 (2015) 166–180, https://doi.org/10.1016/j.apcatb.2014.11.019.

[27] H.L. Huynh, J. Zhu, G. Zhang, Y. Shen, W.M. Tucho, Y. Ding, et al., Promoting effect of FE on supported Ni catalysts in CO2 methanation by in situ DRIFTS and DFT study, J. Catal. 392 (2020) 266–277, https://doi.org/10.1016/j.jcat.2020.10.018.

[28] J. Goldwasser, A study of the platinum-germanium catalytic system, J. Catal. 100 (1986) 75–85, https://doi.org/10.1016/0021-9517(86)90073-4.

[29] D. Zagorac, H. Müller, S. Ruehl, J. Zagorac, S. Rehme, Recent developments in the inorganic crystal structure database: theoretical crystal structure data and related features, J. Appl. Cryst. 52 (2019) 918–925, https://doi.org/10.1107/S160057671900997X.

[30] H. Nasu, D. Hirota, K. Inoue, T. Hashimoto, A. Ishihara, Luminescent properties of amorphous Al2O3 prepared by sol-gel method, J. Ceram. Soc. Jpn. 116 (2008) 835–836, https://doi.org/10.2109/jcersj2.116.835.

[31] A.MD. Rodiansono, D.R. Mujiyanti, U.T. Santoso, S. Shimazu, Novel preparation method of bimetallic Ni-In alloy catalysts supported on amorphous alumina for the highly selective hydrogenation of furfural, Mol. Catal. 445 (2018) 52–60, https://doi.org/10.1016/j.mcat.2017.11.004.

[32] X. Lin, H. Zhu, M. Huang, C. Wan, D. Li, L. Jiang, Controlled preparation of Ni–Cu alloy catalyst via hydrotalcite-like precursor and its enhanced catalytic performance for methane decomposition, Fuel Process. Technol. 233 (2022) 107271, https://doi.org/10.1016/j.fuproc.2022.107271.

[33] B. Ali, S. Tasirin, P. Aminayi, Z. Yaakob, N. Ali, W. Noori, Non-supported nickel-based coral sponge-like porous magnetic alloys for catalytic production of syngas and carbon bio-nanofilaments via a biogas decomposition approach, Nanomaterials 8 (2018) 1053, https://doi.org/10.3390/nano8121053.

[34] K. Sakamoto, F. Hayashi, K. Sato, M. Hirano, N. Ohtsu, XPS spectral analysis for a multiple oxide comprising NiO, TiO2, and NiTiO3, Appl. Surf. Sci. 526 (2020) 146729, https://doi.org/10.1016/j.apsusc.2020.146729.

[35] E.S. Lambers, C.N. Dykstal, J.M. Seo, J.E. Rowe, P.H. Holloway, Room-temerature oxidation of Ni(110) at low and atmospheric oxygen pressures, Oxid. Met. 45 (1996) 301–321, https://doi.org/10.1007/BF01046987.

[36] T. Uchikoshi, Y. Sakka, M. Yoshitake, K. Yoshihara, A study of the passivating oxide layer on fine nickel particles, Nanostruct. Mater. 4 (1994) 199–206, https://doi.org/10.1016/0965-9773(94)90078-7.

[37] S. Wang, J. Wang, X. Ji, J. Meng, Y. Sui, F. Wei, et al., Formation of hollow-cubic Ni(OH)2/CuS2 nanocomposite via sacrificial template method for high performance supercapacitors, J. Mater. Sci. Mater. Electron. 31 (2020) 10489–10498, https://doi.org/10.1007/s10854-020-03597-z.

[38] O. Phichairatanaphong, Y. Poo-Arporn, M. Chareonpanich, W. Donphai, Effect of calcination temperature on cu-modified Ni catalysts supported on mesocellular silica for methane decomposition, ACS Omega 7 (2022) 14264–14275, https://doi.org/10.1021/acsomega.2c01016.

[39] S. Li, J. Tang, Q. Liu, X. Liu, B. Gao, A novel stabilized carbon-coated nZVI as heterogeneous persulfate catalyst for enhanced degradation of 4-chlorophenol, Environ. Int. 138 (2020) 105639, https://doi.org/10.1016/j.envint.2020.105639.

[40] Thermo Fisher Scientific Inc. Iron: Iron X-ray photoelectron spectra, iron electron configuration, and other elemental information. 2023. https://www.thermofisher.com/uk/en/home/materials-science/learning-center/periodic-table/transition-metal/iron.html (accessed September 15, 2023).

[41] T. Yoon, H. Shao, R. Weissleder, H. Lee, Oxidation kinetics and magnetic properties of elemental iron nanoparticles, Part. Part. Syst. Char. 30 (2013) 667–671, https://doi.org/10.1002/ppsc.201300013.

[42] C. Gattinoni, A. Michaelides, Atomistic details of oxide surfaces and surface oxidation: the example of copper and its oxides, Surf. Sci. Rep. 70 (2015) 424–447, https://doi.org/10.1016/j.surfrep.2015.07.001.

[43] Reddy PH, Kir'yanov A V., Dhar A, Das S, Dutta D, Pal M, et al. Fabrication of ultra-high numerical aperture GeO 2 -doped fiber and its use for broadband supercontinuum generation: publisher's note . Appl Opt 2022;61:10229. https://doi.org/10.1364/ao.481300.

[44] F. Sgarbossa, Germanium monolayer doping: successes and challenges for the next generation Ge devices, Mater. Sci. Semicond. Process. 167 (2023) 107795, https://doi.org/10.1016/j.mssp.2023.107795.

[45] J. Xu, G.F. Froment, Methane steam reforming, methanation and water-gas shift: I. Intrinsic Kinetics, Aiche J. 35 (1989) 88–96, https://doi.org/10.1002/aic.690350109.

[46] D. Pashchenko, Intra-particle diffusion limitation for steam methane reforming over a Ni-based catalyst, Fuel 353 (2023) 129205, https://doi.org/10.1016/j.fuel.2023.129205.

[47] T. Miyata, M. Shiraga, D. Li, I. Atake, T. Shishido, Y. Oumi, et al., Promoting effect of Ru on Ni/Mg(Al)O catalysts in DSS-like operation of CH4 steam reforming, Catal. Commun. 8 (2007) 447–451, https://doi.org/10.1016/j.catcom.2006.07.018.

[48] T. Miyata, D. Li, M. Shiraga, T. Shishido, Y. Oumi, T. Sano, et al., Promoting effect of Rh, Pd and Pt noble metals to the Ni/Mg(Al)O catalysts for the DSS-like operation in CH4 steam reforming, Appl. Catal. A 310 (2006) 97–104, https://doi.org/10.1016/j.apcata.2006.05.022.

[49] M. Nawfal, C. Gennequin, M. Labaki, B. Nsouli, A. Aboukaïs, E. Abi-Aad, Hydrogen production by methane steam reforming over Ru supported on Ni–Mg–Al mixed oxides prepared via hydrotalcite route, Int. J. Hydrogen Energy 40 (2015) 1269–1277, https://doi.org/10.1016/j.ijhydene.2014.09.166.

[50] L. Yin, X. Chen, M. Sun, B. Zhao, J. Chen, Q. Zhang, et al., Insight into the role of Fe on catalytic performance over the hydrotalcite-derived Ni-based catalysts for CO2

methanation reaction, Int. J. Hydrogen Energy 47 (2022) 7139–7149, https://doi.org/10.1016/j.ijhydene.2021.12.057.
[51] A.S. Al-Fatesh, A.H. Fakeeha, A.A. Ibrahim, W.U. Khan, H. Atia, R. Eckelt, et al., Decomposition of methane over alumina supported Fe and Ni–Fe bimetallic catalyst: effect of preparation procedure and calcination temperature, J. Saudi Chem. Soc. 22 (2018) 239–247, https://doi.org/10.1016/j.jscs.2016.05.001.
[52] D. Pashchenko, I. Makarov, Carbon deposition in steam methane reforming over a Ni-based catalyst: experimental and thermodynamic analysis, Energy 222 (2021) 119993, https://doi.org/10.1016/j.energy.2021.119993.
[53] P. Zang, J. Tang, X. Zhang, L. Cui, J. Chen, P. Zhao, et al., Strategies to improve CaO absorption cycle stability and progress of catalysts in Ca-based DFMs for integrated CO2 capture-conversion: a critical review, J. Environ. Chem. Eng. 11 (2023) 111047, https://doi.org/10.1016/j.jece.2023.111047.
[54] D.L. Trimm, Coke formation and minimisation during steam reforming reactions, Catal. Today 37 (1997) 233–238, https://doi.org/10.1016/S0920-5861(97)00014-X.
[55] J. Sun, X. Jin, F. Zhang, W. Hu, J. Liu, R. Li, Ni–Cu/γ-Al2O3 catalyzed N-alkylation of amines with alcohols, Catal. Commun. 24 (2012) 30–33, https://doi.org/10.1016/j.catcom.2012.03.010.
[56] E. Gioria, P. Ingale, F. Pohl, R. Naumann d'Alnoncourt, A. Thomas, F. Rosowski, Boosting the performance of Ni/Al $_{2}$ O 3 for the reverse water gas shift reaction through formation of CuNi nanoalloys, Cat. Sci. Technol. 12 (2022) 474–487, https://doi.org/10.1039/D1CY01585K.
[57] H. Wu, L. Guo, F. Ma, Y. Wang, W. Mo, X. Fan, et al., Structure and surface characteristics of Fe-promoted Ni/Al $_{2}$ O 3 catalysts for hydrogenation of 1,4-butynediol to 1,4-butenediol in a slurry-bed reactor, Cat. Sci. Technol. 9 (2019) 6598–6605, https://doi.org/10.1039/C9CY01195A.
[58] J. Kumar Prabhakar, P.A. Apte, G. Deo, The kinetics of Ni/Al2O3 and Ni-Fe/Al2O3 catalysts for the CO2 methanation reaction and the reasons for promotion, Chem. Eng. J. 471 (2023) 144252, https://doi.org/10.1016/j.cej.2023.144252.
[59] G.S. Dhillon, G. Cao, N. Yi, The role of Fe in Ni-Fe/TiO2 catalysts for the dry reforming of methane, Catalysts 13 (2023) 1171, https://doi.org/10.3390/catal13081171.
[60] N. Bayat, M. Rezaei, F. Meshkani, Methane decomposition over Ni–Fe/Al2O3 catalysts for production of COx-free hydrogen and carbon nanofiber, Int. J. Hydrogen Energy 41 (2016) 1574–1584, https://doi.org/10.1016/j.ijhydene.2015.10.053.
[61] X. Xu, S. Kumar Megarajan, X. Xia, A. Toghan, A. Feldhoff, Y. Zhang, et al., Effect of reduction temperature on the structure and catalytic performance of mesoporous Ni–Fe–Al_2O_3 in oxidative dehydrogenation of ethane, New J. Chem. 44 (2020) 18994–19001, https://doi.org/10.1039/D0NJ02618B.
[62] Sabatier P. La catalyse en chimie organique. vol. 3. C.Beranger; 1920.
[63] A.J. Medford, A. Vojvodic, J.S. Hummelshøj, J. Voss, F. Abild-Pedersen, F. Studt, et al., From the Sabatier principle to a predictive theory of transition-metal heterogeneous catalysis, J. Catal. 328 (2015) 36–42, https://doi.org/10.1016/j.jcat.2014.12.033.
[64] F. Studt, F. Abild-Pedersen, Q. Wu, A.D. Jensen, B. Temel, J.-D. Grunwaldt, et al., CO hydrogenation to methanol on Cu–Ni catalysts: theory and experiment, J. Catal. 293 (2012) 51–60, https://doi.org/10.1016/j.jcat.2012.06.004.